JOURNAL OF MATERIALS SCIENCE **39** (2004) 5959–5968

Microhardness and high-velocity impact resistance of HfB_2/SiC and ZrB_2/SiC composites

J. MARSCHALL
Molecular Physics Laboratory, SRI International, Menlo Park, CA 94025, USA
E-mail: jochen.marschall@sri.com

D. C. ERLICH
Materials Research Laboratory, SRI International, Menlo Park, CA 94025, USA

H. MANNING, W. DUPPLER
Physics Department, Concordia College, Moorhead, MN 56562, USA

D. ELLERBY
Thermal Protection Materials and Systems Branch, NASA Ames Research Center, Moffett Field, CA 94035, USA

M. GASCH
ELORET Corp. at NASA Ames Research Center, Moffett Field, CA 94035, USA

The results of Vickers microhardness and high-velocity impact tests on monolithic ZrB_2/SiC and HfB_2/SiC ultra-high temperature ceramic (UHTC) composites are presented. The UHTC materials exhibit fracture behavior typical of ceramics under indentation and impact loading. The materials are relatively hard with microhardness values of about 15 to 20 GPa. Cracks were observed to extend from the corners of indentations. Impacts of stainless steel and tungsten carbide spheres, with diameters in the 500 to 800 micron range and velocities of 200 to 300 m/s, produced minimal plastic deformation but significant radial and ring cracking at the impact sites. Impacts of micron-scale iron particles traveling at 1 to 3 km/s produced essentially no surface damage.

1. Introduction

Hypersonic flight vehicle designs incorporating sharp leading edges have many potential advantages over traditional blunt-body designs. These advantages derive primarily from higher lift to drag ratios that translate into increased cross-range capability, improved high-speed maneuverability, better landing characteristics, and a greater ability to fly abort or emergency trajectories. As one example, recent modeling studies comparing the performance of blunt-body and sharp-body designs for a crew transfer vehicle to ferry astronauts between the Earth and the International Space Station found dramatic performance benefits for the sharp-body design [1, 2].

Sharp leading edges experience intense aerothermal heating that few materials can survive. Monolithic ultra-high temperature ceramic (UHTC) composites based on ZrB_2 and HfB_2 offer a potential solution. Both the diborides and their primary metal oxides have extremely high melting points [3]. UHTC composites have shown good dimensional stability in low-pressure supersonic aerothermal heating environments, where other refractory materials rapidly fail by melting, spalling, pyrolyzing or ablating [4]. Several studies have demonstrated that the high-temperature oxidation/ablation resistance of diboride-based UHTC materials is enhanced by the addition of SiC [5–9], with optimum performance achieved around 20 vol% SiC. UHTC leading edge components were flown by NASA in two separate hypersonic flight tests, SHARP-B1 (1997; UHTC nose tip) [10, 11] and SHARP-B2 (2000; UHTC strakes).

In this paper, we present the results of some preliminary experiments exploring the hardness and impact resistance of UHTC materials. Impact damage is a major concern for any leading edge component, since leading edges are exposed to the most severe aerothermal environments and directly influence vehicle flight characteristics. A very large spectrum of possible impacts exists, ranging from tool drops, to collisions with high velocity debris during take-off and landing, to hypervelocity impacts with micrometeorites and "space junk" while in-orbit. We sample some of these impact conditions, using a compressed gas gun to fire steel and tungsten carbide balls with diameters of $\sim$0.5 mm at velocities in the 100–300 m/s range, and a 2 MV Van de Graaff particle accelerator to fire micron-scale iron particles in the 1–3 km/s range. We document the results using optical and scanning electron microscopy.

2. Experimental procedure

2.1. UHTC materials

Experiments were conducted on two UHTC compositions: ZrB_2 with 20 vol% SiC and HfB_2 with 20 vol% SiC. The former composition has a density of ~5.5 g/cm^3 and latter of ~9.5 g/cm^3. For brevity, these two compositions are referred to as ZrB_2/SiC and HfB_2/SiC throughout the text. UHTC materials are manufactured from diboride and silicon carbide powders, by hot pressing. All materials were supplied by NASA Ames Research Center, either from remaining stock manufactured during the SHARP-B1 and SHARP-B2 programs by commercial vendors, or from newer material manufactured in-house at NASA Ames. The former materials are referred to as "heritage" materials and the later as "current" materials in the text. Test samples were machined from the billets using diamond cutting and grinding operations, and polished using diamond powder.

2.2. Microhardness measurements

The Vickers microhardness of UHTC samples was measured at SRI using a Leitz Durimet Small-Hardness tester and at NASA Ames using a Shimadzu HSV-30 hardness tester. Measurement consistency between the two hardness testers was verified experimentally. Measurements at SRI were made with a constant load of 19.6 N (2 kg mass), while data at NASA Ames was gathered under a variety of loads ranging from 1.96 to 294 N (0.2–30 kg mass). Indentations were examined using optical and scanning electron microscopy.

2.3. Gas gun impact experiments

UHTC samples were impacted with tungsten carbide or stainless steel balls using a compressed gas gun. Type 44A tungsten carbide (WC) balls with diameters of 794 μm (1/32 inch) and 508 μm (0.020 inch), and type 440-C stainless steel (SS) balls with diameters of 508 μm (0.020 inch) and 762 mm (0.030 inch), were used. The tolerances on ball diameters are ±5 μm. Type 44A WC contains 6% cobalt by weight. Both materials are magnetic. The pertinent physical properties of these balls are given in Table I.

TABLE I Physical properties of tungsten carbide and stainless steel spheres[a]

	WC 44A	SS 440-C
ρ (g/cm^3)	14.95	7.67
v	0.26	0.29
E (GPa)	690	200
H_R	C58–C65	A90.5–A91.5

[a] Manufacturer data; New England Miniature Ball Corporation (www.nemb.com).

Fig. 1 shows the essential components of the gas gun apparatus. A single ball is placed into the gun barrel and held in place by a magnet. The ball is accelerated down the barrel by the sudden release of a compressed gas (nitrogen). The gas is released either by opening a valve or by rupturing a thin diaphragm separating the barrel from a compressed gas reservoir. The accelerated ball is sequentially detected by three photodiodes as it travels down the gun barrel, and its velocity is calculated from the measured time intervals and the known photodiode spacing. Velocities are varied by changing the type and thickness of the diaphragm or by adjusting the pressure in the gas reservoir.

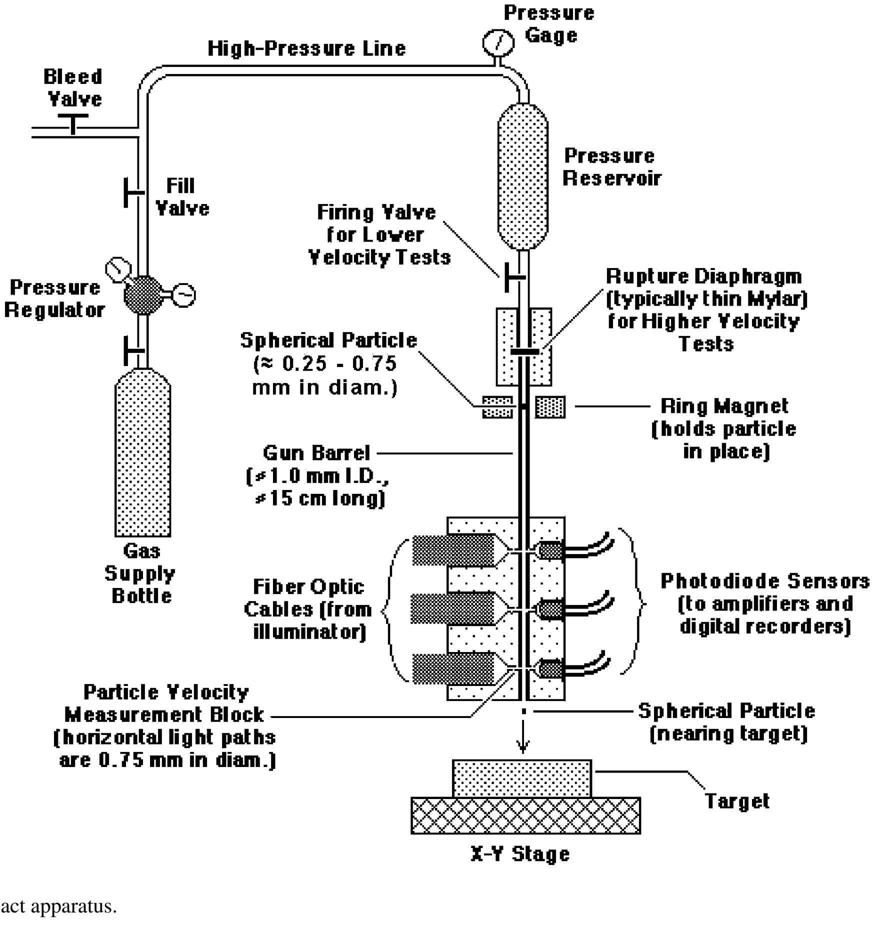

Figure 1 Gas gun impact apparatus.

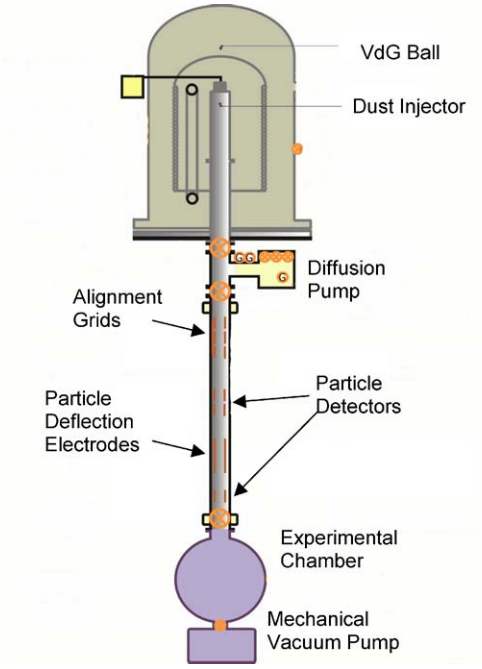

Figure 2 Van de Graaff particle accelerator.

2.4. Particle accelerator impact experiments

The resistance of UHTC samples to hypervelocity impact by micron-sized iron particles was explored using a 2 MV Van de Graaff particle accelerator located at Concordia College, in Moorhead, Minnesota. Fig. 2 shows a schematic diagram of the particle accelerator. Particles are loaded into an injector inside the Van de Graaff ball. The injector agitates the dust, generating a dust cloud. Some particles contact a sharp needle maintained at high voltage and acquire a large positive charge. These particles are then focused, injected into the electric field of the Van de Graaff, and accelerated downstream. After leaving the Van de Graaff ball, the particles travel through a field-free drift tube, where sensors measure the velocity and charge of individual particles. Knowledge of these quantities together with the accelerator voltage allow calculation of the particle mass, and for spherical particles with a known density, the particle diameter. A test chamber is positioned at the end of the flight tube, where particles are directed at a target for impact testing. Particles not meeting user-chosen specifications of charge and velocity can be deflected before entering the test chamber.

Efficient particle charging and acceleration requires conductive particles. Past experience has shown that micron-sized iron particles, manufactured from iron carbonyl by a reduction process, work well in the accelerator. Such particles were also used in the present tests. Unfortunately, the carbonyl reduction process results in substantial particle porosity and somewhat uncertain particle density in the 4 to 6 g/cm^3 range. The hardness of these particles is also uncertain.

3. Results

3.1. Microhardness measurements

Vickers microhardness measurements were made at SRI on heritage HfB_2/SiC and ZrB_2/SiC specimens. Fifteen individual measurements were made at a load of 19.6 N on each specimen and examined optically. Average microhardness values were 20.5 ± 1.6 GPa for the HfB_2/SiC sample and 18.1 ± 1.0 GPa for the ZrB_2/SiC sample. A typical impression on ZrB_2/SiC is shown in the SEM image of Fig. 3. Cracks are observed to extend from the indentation corners and some chipping is seen along indentation edges. The extent of cracking was generally less, and the extent of chipping more, in the HfB_2/SiC specimens. Cracks propagate both around and through individual grains, while chipping appears to be associated mainly with failure along grain boundaries.

A series of Vickers microhardness indentations were made as a function of load at NASA Ames Research Center on two samples of current HfB_2/SiC material.

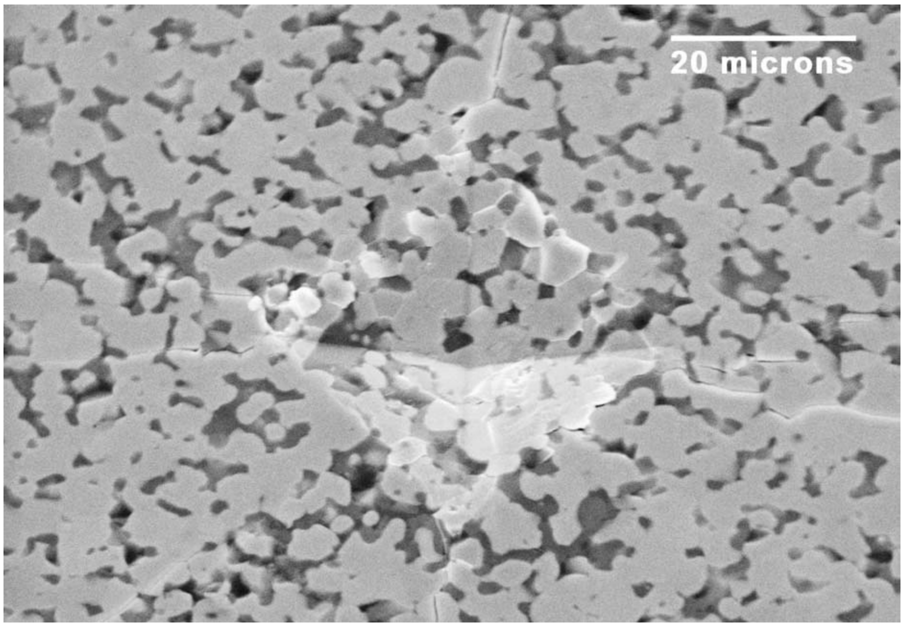

Figure 3 SEM image of a Vickers microhardness impression on heritage ZrB_2/SiC. Light grains are ZrB_2 and dark grains SiC.

TABLE II Published microhardness values for ZrB_2, HfB_2 and SiC

Material	Microhardness (GPa)	Comments
ZrB_2	35.0[a]	Vickers, polycrystal
	29.4[b]	Vickers, 50 g load, single grains
	∼25–30[c]	Knoop, single crystal, anisotropic effects
	22.1[d]	–
HfB_2	31.4[b]	Vickers, 50 g load, single grains
	∼25–30[c]	Knoop, single crystal
SiC	31.0[a]	Vickers, single crystal
	27.0[a]	Vickers, polycrystal
	28.2[d]	Knoop, 25 g load
	27.2[e]	Vickers, 500 g load, sintered α-SiC
	25[f]	Knoop, load-independent, 6H-SiC film

[a]Milman *et al.* [26]; [b]Bsenko and Lundström [27]; [c]Nakano *et al.* [28]; [d]Glazov and Vigdorovich [29]; [e]Quinn *et al.* [30]; [f]Kakanakova-Georgieva *et al.* [31].

Impressions produced under a 9.81 N load have indentation diagonals on the order of 30 μm. At lower loads, impression dimensions begin to approach the scale of the microstructure and are highly distorted by cracking or chipping of individual grains. Hardness values did not vary significantly or systematically with increasing loads above 9.81 N. Averaging the measurements obtained at 9.81, 29.4, 49, 98.1, and 294 N, gives 16.3 ± 0.4 GPa and 15.4 ± 0.3 GPa for the two HfB_2/SiC specimens. The current HfB_2/SiC material appears to be somewhat softer than the heritage material, though still quite hard by comparison to most other materials.

Our microhardness values can be compared with various data reported in the literature for ZrB_2, HfB_2 and SiC, and summarized in Table II. Our measured microhardness values for the ZrB_2/SiC and HfB_2/SiC composites are generally lower than literature values for the individual constituents.

3.2. Gas gun impact results

Fifty-five separate shots were fired at normal incidence at 14 different UHTC samples. Not all of the shots could be correlated to damage on the surface. Generally, impact velocities of ∼200 m/s on ZrB_2/SiC and ∼250 m/s on HfB_2/SiC were required before impact sites could be positively identified on polished specimens using optical microscopy or SEM imaging. Only one of the nine impacts below these velocity thresholds was identified, a 94 m/s, 794 μm WC sphere impact on ZrB_2/SiC. While impact damage below these velocity thresholds is likely, the difficulty in locating and identifying such impact site also reflects the limited surface damage done to these materials at the lower impact velocities.

Fig. 4 shows an impact site produced by a 794 μm WC ball striking a heritage ZrB_2/SiC specimen at 308 m/s. A concentric ring crack pattern is formed and radial cracks extend outward. These types of cracking patterns are the major visual indicators of impact damage. No evidence of UHTC material removal by fragmentation was found. The dark objects surrounding the impact site were confirmed by EDX analysis to be fragments from the impacting WC ball.

The largest ring crack diameter in Fig. 4 is about 500 μm. Myriad concentric ring cracks lie within this bounding diameter. SEM images of this area show tightly spaced ring cracks that appear as thin, white traces with no visible separation between adjacent surfaces; see Fig. 5. The concentric ring pattern suggests displacements into the surface to accommodate the spherical particle impact. The lack of separation between adjacent crack surfaces suggests a locally compressive stress field normal to the surface traces.

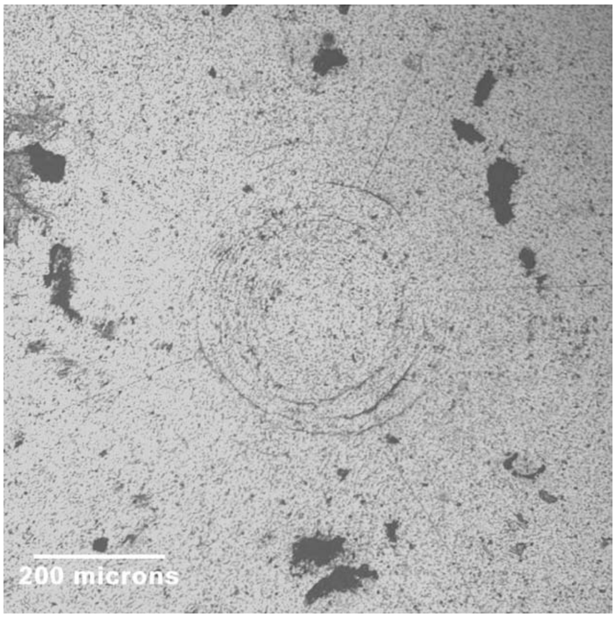

Figure 4 Optical microscope image of surface damage produced on a heritage ZrB_2/SiC surface by the 308 m/s impact of a 794 μm diameter tungsten carbide ball.

In contrast, radial cracks generally appear more open, with mating surfaces visibly separated, suggesting a local tensile stress. Fig. 6 shows an SEM image of a radial crack extending from the outer ring crack pattern. Though difficult to trace to their terminus, many radial cracks were observed to extend at least 2 to 5 times the outer ring crack diameter.

The nature and extent of the crack patterns generated around impact sites varies. Fig. 7 summarizes the diameters of the outer most ring crack observed on ZrB_2/SiC and HfB_2/SiC surfaces as a function of velocity for impacting spheres with different sizes and compositions. Similar plots can be made as a function of impact momentum and kinetic energy. Measurements of crack dimensions are somewhat subjective, but some general observations can be made.

Impacts by balls of comparable size, composition and velocity produced more extensive damage to ZrB_2/SiC than to HfB_2/SiC, as reflected by the quantity and extent of the observed surface cracks.

Impacts with stainless steel spheres left fundamentally different surface patterns than tungsten carbide spheres. Instead of numerous concentric ring cracks, as seen in Fig. 4, stainless steel impacts typically produced a single prominent ring crack, as shown in Fig. 8. The ring crack in Fig. 8 is a perfect 595 μm diameter circle. Only for the highest velocity impacts, on ZrB_2/SiC, was there any evidence of multiple ring cracks produced by stainless steel impacts, and the additional cracks were still bounded by a prominent outer ring crack.

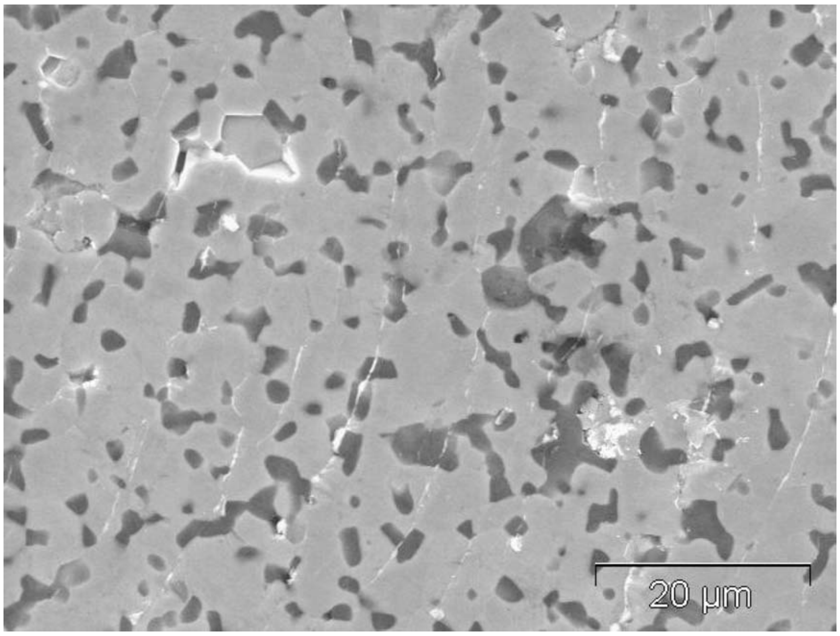

Figure 5 SEM image of ring crack pattern on ZrB_2/SiC surface; same impact as Fig. 4.

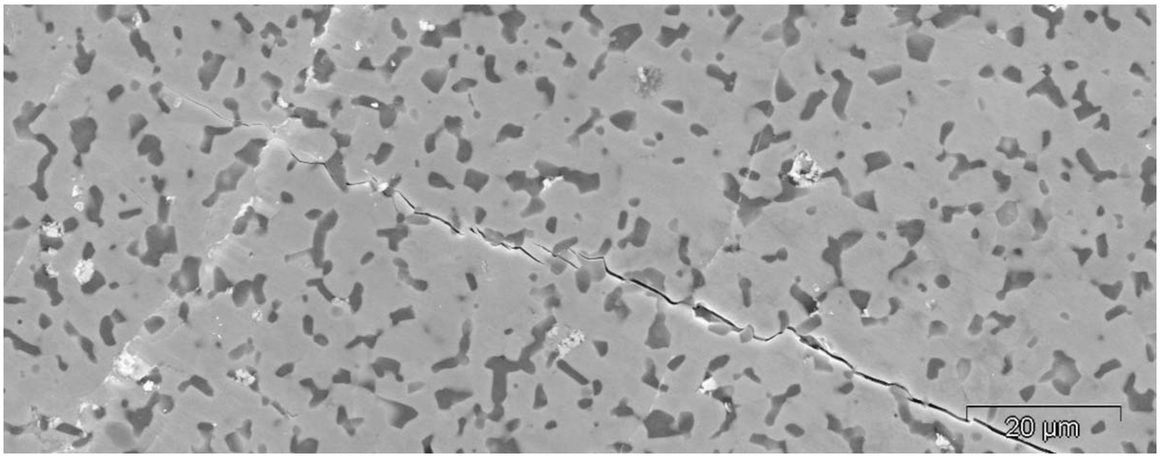

Figure 6 SEM image of a radial crack at boundary of ring crack pattern on ZrB_2/SiC surface; same impact as Fig. 4.

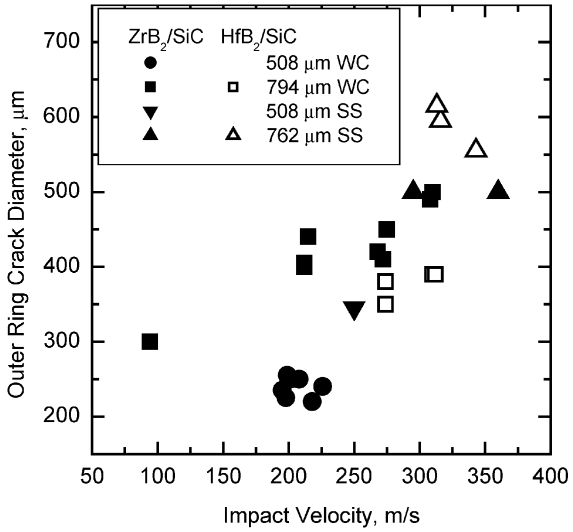

Figure 7 Summary of outer ring crack diameters observed on ZrB_2/SiC and HfB_2/SiC surfaces as a function of size, composition, and velocity of the impacting ball.

None of the stainless steel impacts produced observable radial cracks on either ZrB_2/SiC or HfB_2/SiC surfaces. Neither did impacts of 508 μm WC spheres on ZrB_2/SiC. The formation of radial cracks evidently requires more energetic impacts than the formation of ring cracks. In our experiments only the highest speed impacts (over ∼250 m/s) with the large WC balls produced radial cracks that extend away from the concentric ring crack pattern.

A computer-controlled scanning laser confocal microscope [12] was used to obtain orthogonal surface profiles of impressions made by 310 m/s impacts of 794 μm diameter WC spheres on ZrB_2/SiC and HfB_2/SiC; see Fig. 9. These profiles reveal greater residual deformation in the ZrB_2/SiC specimen. The profiles show more extrusion of material around the impact on the ZrB_2/SiC surface, and the impression depth in the ZrB_2/SiC is 30 to 40% greater than in the HfB_2/SiC. These findings are in line with the qualitative observation that impressions made by comparable

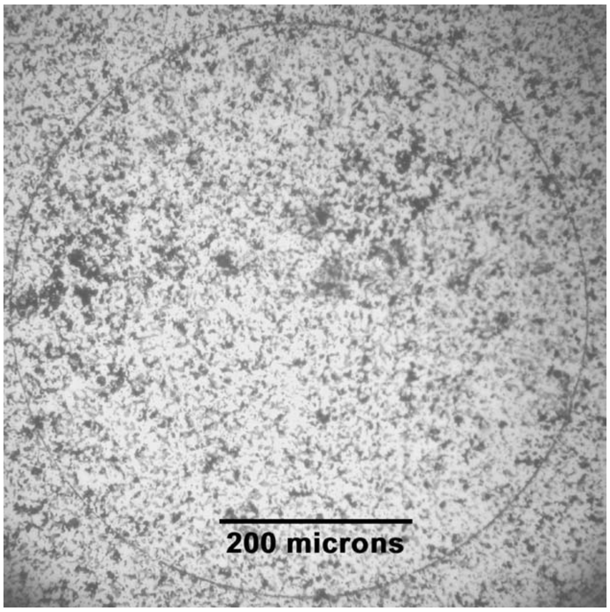

Figure 8 Optical microscope image of the ring crack generated by the 316 m/s impact of a 762 μm diameter stainless steel ball on a HfB_2/SiC surface.

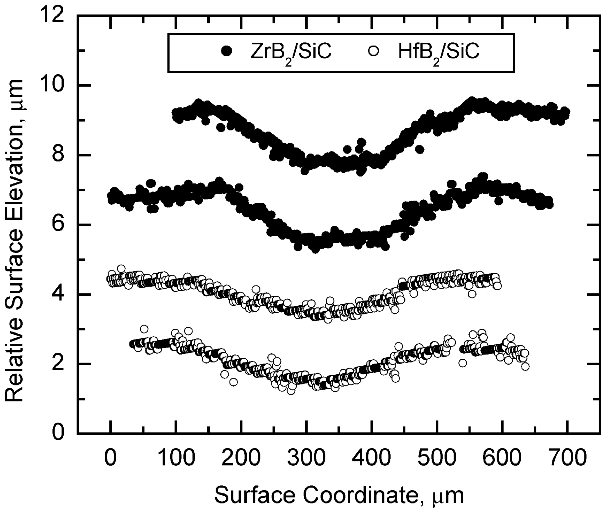

Figure 9 Orthogonal surface profiles through the centers of impressions produced by 310 m/s impacts of 794 μm diameter WC spheres on ZrB_2/SiC and HfB_2/SiC surfaces. Profiles are separated by arbitrary elevation offsets for clarity.

impacts were easier to detect visually using oblique illumination on the ZrB_2/SiC specimens.

The effect of impact damage on biaxial flexural strength was examined by testing three impacted disks of current HfB_2/SiC material using a standard concentric ring flexural test as described in ASTM standard C 1499-03 [13]. Each disk was impacted with a single 794 mm diameter WC ball, the first at 312 m/s, the second at 206 m/s and the third at an unknown velocity below 100 m/s. The first two disks had an as-ground surface finish, while the latter was polished.

The first and second impacted specimens exhibited fracture strengths of 195 and 226 MPa, respectively. These two values are well below 426 ± 48 MPa, the average fracture strength and standard deviation determined for five un-impacted as-ground test samples. Both the first and second specimen failed in the region of the impact. The third impacted specimen failed in a normal manner directly under the compression ring center, with measured fracture strength of 458 MPa. This value is comparable to 487 ± 35 MPa, the average fracture strength and standard deviation measured for five un-impacted polished test samples.

All fractures were clean from processing defects, agglomerates, and inclusions. The test results suggest that microcrack formation, induced by particle impact, weakened the first and second specimens noticeably, while the impact velocity was too low to cause significant damage to the third specimen.

3.3. Particle accelerator impact results

Several HfB_2/SiC and ZrB_2/SiC specimens were impacted at normal and oblique incidence by carbonyl iron particles with diameters around 1 micron traveling at speeds around 1.8 km/s. Table III summarizes the pertinent experimental parameters for these tests.

At normal incidence, particle impacts, detected by SEM in the form of surface abnormalities, were found on both the ZrB_2/SiC and the HfB_2/SiC specimens. Many more residual iron particles were found on ZrB_2/SiC than HfB_2/SiC, though this discrepancy may partially reflect the greater number of particles fired at the former specimen. Fig. 10 shows an example of two such impact sites on ZrB_2/SiC. Visually, these sites appear to show deformed iron particles that have adhered to the specimen surface. Stereo images of various impact sites, produced from SEM micrographs obtained at different specimen tilt angles, indicate that the impact features extend above the sample surface.

Fig. 10 also shows local EDX spectra taken at the four different locations on the impact sites as indicated in the SEM micrograph. The prominent iron peaks at sites 1, 2, and 3 confirm that the impact features are indeed residual iron particles. The EDX technique probes a surface depth on the order of a micron. Si and Zr peaks associated with the surface material beneath the residual iron are also present, suggesting that residual iron layer is considerably thinner than a micron.

Unambiguous detection of impact damage to UHTC specimens was difficult. No extended damage, such as surface cracks emanating from impact sites, was ever

TABLE III Experimental parameters for UHTC impact tests using the Van de Graaff particle accelerator

	Test 1	Test 2	Test 3	Test 4
Specimen	HfB_2/SiC	HfB_2/SiC	ZrB_2/SiC	ZrB_2/SiC
Incident angle (deg)	0	70	0	70
Number of shots	200	150	400	800
Velocity (km/s)				
Average	1.75 ± 0.46	1.87 ± 0.46	1.76 ± 0.72	1.82 ± 0.47
Median	1.66	1.82	1.66	1.74
Mass (pg)				
Average	44.4 ± 61.5	28.5 ± 36.8	49.2 ± 66.04	38.8 ± 53.2
Median	25.3	15.5	27.0	20.6
Kinetic energy (nJ)				
Average	45 ± 38	35 ± 29	48 ± 40	42 ± 37
Median	37	28	36	32

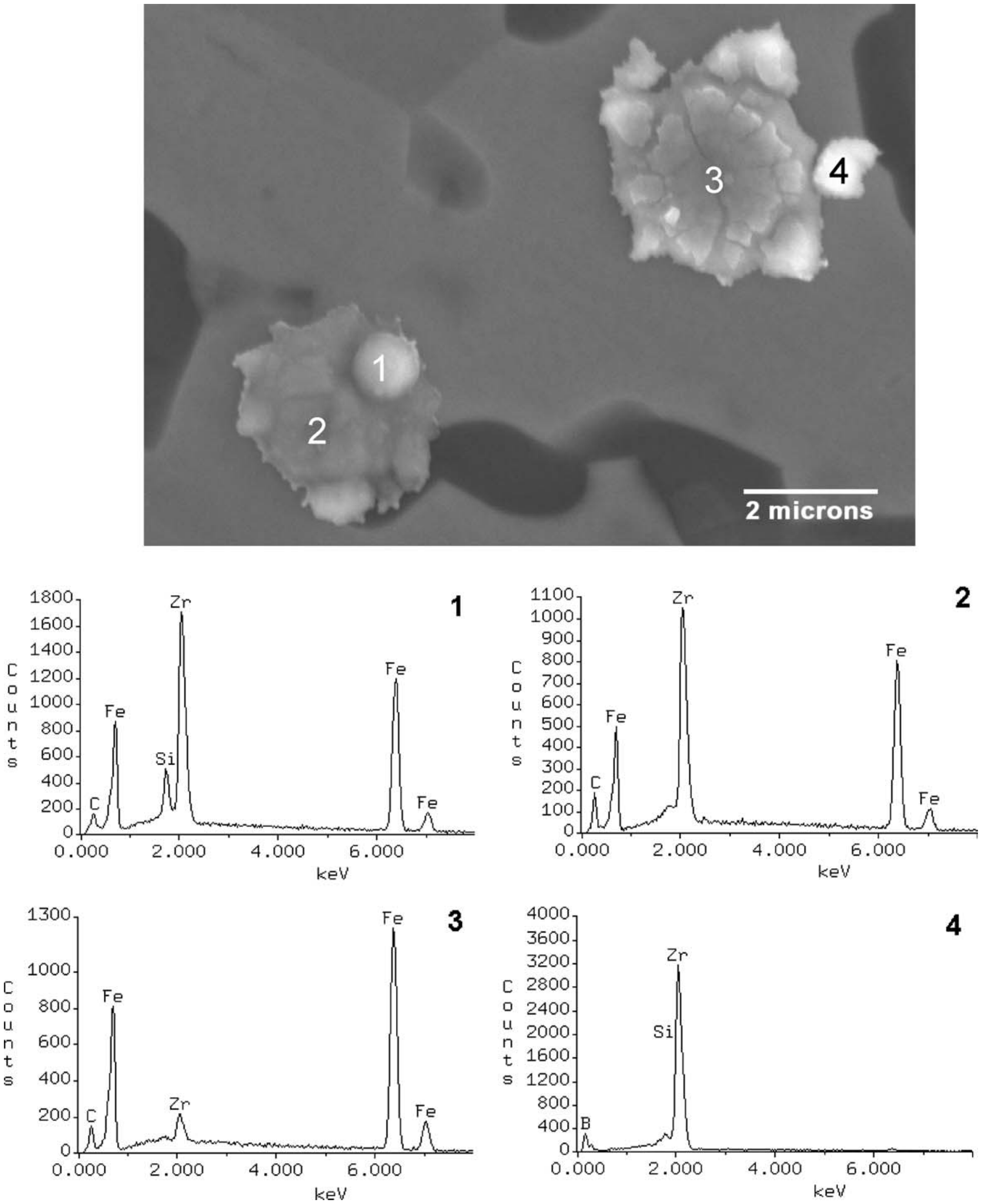

Figure 10 SEM micrograph showing two impact sites of micron-sized carbonyl iron particles on a ZrB_2/SiC surface, along with the EDX spectra obtained at the four locations indicated.

observed. At most sites the UHTC materials seem completely unaffected by the impact. In some cases, like location 3 in Fig. 10, the central region of an impact site exhibits a "fragmentary" pattern that suggests impact damage to the UHTC. However, EDX spectra of these regions show strong iron signals, so it seems more likely the patterns reflect the deformation of impacting iron particles rather than damage to the UHTC below. Nevertheless, some damage to UHTC material was occasionally found. For, example, the EDX spectrum taken at location 4 shows no iron peaks and strong Zr and B peaks, suggesting a ZrB_2 fragment was created during the impact.

At oblique incidence, no particle impacts could be detected. The location of oblique impact sites by SEM is expected to be more difficult, since the impacts are spread out over a larger target area ($\sim$3 times larger for an incident angle of 70°.) However, for the ZrB_2/SiC experiments, the diluting effect of the increased target area was largely offset by doubling the number of impacting particles. Therefore, it seems more likely that particles are deflected by their oblique collisions with the surface.

In a further experiment, a ZrB_2/SiC specimen was impacted at normal incidence in two separate locations by approximately 100 particles traveling either 1.0 to 1.3 km/s or greater than 2 km/s. Some impact sites, such as the left impact in Fig. 10, show droplet features that hint at melting. A simple analysis indicates that about 1.25 MJ/kg of thermal energy will completely melt an iron particle initially at room temperature. Iron particles traveling faster than ~1.6 km/s generally posses kinetic energies per mass in excess of this value. For the slow particle group, the specific kinetic energy ranged from 0.43 to 0.89 MJ/kg and for the fast group 1.9 to 5.0 MJ/kg. SEM and EDX observations revealed numerous impact sites with adhering iron material for the slower particles, but none for the faster particles. Thus complete particle melting is not required for surface adhesion and higher impact velocities seem to prevent iron remnants from adhering to the surface.

4. Discussion

The response of ZrB_2/SiC and HfB_2/SiC samples to indentation and particle impact is typical of that observed for ceramics and glasses [14–16]. For point contact on brittle solids, the loading phase typically leads to the formation and growth of a small, highly deformed plastic zone from which median vent cracks are nucleated and extended. The unloading phase results in the additional formation and extension of lateral vent cracks, and closing of the median cracks [14, 17, 18]. The intersection of the median vent cracks with the surface produces radial cracking patterns. The extension and breakout to the surface of lateral vent cracks can lead to significant fragmentation and chipping. For indentation with a Vickers indenter on isotropic solids, the sharp edges of the pyramidal indenter tend to align median vent cracks with the indentation diagonals and tend to promote more extensive radial cracking [15]. The unloading of a pyramidal indenter also leads to closure of median cracks beneath the indentation, however the near surface region generally experiences tensile stresses that tend to open up and extend radial cracks [15, 19].

Although we do not observe median vent crack formation directly, radial cracks emerging from impression corners are a ubiquitous feature of Vickers indentations on ZrB_2/SiC and HfB_2/SiC samples. No evidence of lateral vent cracks intersecting the surface was found. When chipping was observed, it was in the immediate indentation area and could be associated with the pop-out of individual grains or local fracture around several grains. The emergence of lateral cracks to the surface would be expected at larger distances from the impression and would result in larger fragments than observed.

Contact between a hard blunt indenter and a flat isotropic brittle material can result in loading conditions that are essentially elastic. Under such conditions, Hertzian cone cracks can form, initiating at the surface as ring fractures and then propagating into the material along conical trajectories [20, 21]. Under large concentrated contact pressures, such as for small spherical indenters, plastic deformation may also occur, inhibiting cone cracking and generating the crack types usually associated with sharp indenters [15, 22]. The cracking patterns generated by high-speed impact of spherical particles in the 100's of m/s range are very similar to those found under blunt indenters [15, 20, 22, 23].

The damage observed on ZrB_2/SiC and HfB_2/SiC surfaces for tungsten carbide and stainless steel sphere impacts clearly indicates that loading stresses on the target were predominately elastic. Cone cracking, as evidenced by surface ring crack patterns, is the major fracture mode and is certainly not inhibited by the formation of a plastic zone. The impressions left by impacts are extremely shallow when compared to the size of the impacting spheres. The ratio of impression depth to impacting sphere radius is on the order of 1 to 400 for the profiles shown in Fig. 9, indicating little permanent deformation in the UHTC samples to accommodate the impact stresses. The minimal permanent deformation that is seen is plausibly explained as displacement of material into the surface along cone crack trajectories. The appearance of radial cracks at higher velocities is likely associated with tensile surface hoop stresses formed during unloading.

Formulae based on Hertzian elastic contact theory can be used to estimate the contact radius at maximum load between an impacting sphere and a flat specimen [22]:

$$a = \left(\frac{4}{3}kF_{\max}R\right)^{1/3} \tag{1}$$

where

$$F_{\max} = \left(\frac{5}{3}\pi\rho\right)^{3/5}\left(\frac{3}{4}k\right)^{-2/5} V^{6/5}R^2 \tag{2}$$

and

$$k = \left(\frac{1-v^2}{E} + \frac{1-v_{\text{UHTC}}^2}{E_{\text{UHTC}}}\right). \tag{3}$$

In these expressions, a is the contact radius, $F_{\max}$ is the maximum load, R is the sphere diameter, ρ is the sphere density, V is the sphere velocity and k is a constant related to the Poisson's ratios v, v_{UHTC} and the Young's moduli E, E_{UHTC} of the sphere and the specimen, respectively.

The ZrB_2/SiC and HfB_2/SiC materials both have Poisson's ratios of about 0.15 and Young's moduli [24] of about 530 GPa. Therefore, the predicted contact radius and maximum load are the same on both UHTC compositions for comparable sphere impacts. A contact radius of approximately 18 μm is calculated for the 310 m/s WC impacts profiled in Fig. 9. This is an order of magnitude smaller than the radii of the outer ring cracks generated during the impacts.

Though the contact radius and maximum load are identical, impacts of tungsten carbide spheres generate more extensive ring cracks in ZrB_2/SiC than in HfB_2/SiC at a given velocity. The maximum radial tensile surface stress generated at a distance r from the impact site is given by [22]

$$\sigma_{r,\max} = \frac{(1-2v_{\text{UHTC}})F_{\max}}{2\pi r^2}. \tag{4}$$

If the assumption is made that the outermost ring crack forms where the radial surface stress just exceeds a critical value characteristic of the material, the ratio of critical stresses for the two UHTC formulations can be estimated from

$$\frac{\sigma_{\mathrm{c,HfB_2/SiC}}}{\sigma_{\mathrm{c,ZrB_2/SiC}}} \cong \frac{\left(\frac{V^{6/5}R^2}{r_c^2}\right)_{\mathrm{ave,HfB_2/SiC}}}{\left(\frac{V^{6/5}R^2}{r_c^2}\right)_{\mathrm{ave,ZrB_2/SiC}}}. \tag{5}$$

From the outer ring diameters plotted in Fig. 7 this ratio is about 1.6 ± 0.2.

These computations are only approximate, of course. Some of the available kinetic energy is dissipated in the deformation and fracture of the impacting sphere. Since the heritage HfB_2/SiC is about 1.7 times denser and slightly harder than the heritage ZrB_2/SiC material, it is likely that impacts on HfB_2/SiC result in more energy dissipation into the impacting sphere.

This is very apparent for the SS sphere impacts, which predominately generate a single large ring crack, as shown in Fig. 8. A Rockwell C hardness of 58 to 65 equates approximately to a Vickers hardness of 6.5 to 8 GPa [25], making the stainless steel balls significantly softer than both the heritage ZrB_2/SiC and HfB_2/SiC materials. This must lead to extensive deformation (flattening) of the sphere upon impact. The SS spheres are less dense than, and have the largest hardness discrepancy with the HfB_2/SiC material. For comparable SS impacts, the ring crack diameters are observed to be larger on the HfB_2/SiC material than the ZrB_2/SiC material. This suggests greater deformation of the SS sphere upon impact on the harder and denser material, resulting in a larger contact radius before critical radial surface stress for ring crack formation is exceeded.

A similar deformation mechanism can be invoked to explain the relative lack of surface damage from the micron-scale carbonyl iron particle impacts in the 1 to 3 km/s range. That is, the impact energy is largely dissipated in the deformation and melting of the iron particle, rather than into the UHTC. The density of these iron particles is even lower than that of the SS spheres, and while their hardness is not known exactly, they are likely softer than the UHTC materials.

5. Conclusions

The major findings of this study can be summarized as follows:

1. UHTC materials are relatively hard, with Vicker's hardness numbers in the 15–20 GPa range. Cracks are observed to emanate from indentation corners.
2. Impacts by 508 and 794 μm WC spheres traveling at several 100 m/s produce surface damage observable as patterns of ring and radial cracks. Similar impacts by SS spheres produced considerably less damage.
3. The observed formation of cracks during indentation and particle impact is consistent with damage modes documented for other ceramic materials under similar conditions.
4. Biaxial testing of impacted HfB_2/SiC specimens indicates that impact damage of this sort can cause large decreases in fracture strength.
5. Impacts of micron-sized iron particles traveling at 1 to 3 km/s were shown to cause insignificant damage to UHTC surfaces.

Finally, we note that the experiments presented here are of an exploratory nature. Compared to many other ceramics and glasses, very little is actually known about the impact damage and fracture resistance of ZrB_2/SiC and HfB_2/SiC materials. Further focused investigations should be made to systematically quantify the effect of contact and impact damage on the strength and reliability of UHTC components. The influence of temperature on impact damage should be investigated, since UHTC leading edges will cool well below room temperature on orbit and reach very high surface temperatures during hypersonic flight. Impact experiments with projectiles at orbital velocities (~8 km/s) and above are certainly required to properly assess the risks of imposed by micrometeorites and orbital debris to critical UHTC leading edge components. Finally, the fracture strength degradation observed for the impacted HfB_2/SiC specimens argues strongly for a more extensive testing program to quantify impact induced strength degradation.

Acknowledgements

We thank Scott Payne at the North Dakota State University Electron Microscopy Center for his imaging of the UHTC specimens impacted at Concordia College. We thank Takao Kobayashi of the Materials Research Laboratory at SRI International for profiling several impact sites using laser scanning confocal microscopy.

Jochen Marschall acknowledges support for this work from SRI International through internal research and development funds and from the Air Force Office of Scientific Research through contract F49620-01-C-0026.

References

1. D. SAUNDERS, G. ALLEN, P. GAGE and J. REUTHER, "Crew Transfer Vehicle Trajectory Optimization," AIAA Paper 2001-2885, June 2001.
2. J. REUTHER, D. KINNEY, S. SMITH, D. KONTINOS, P. GAGE and D. SAUNDERS, "A Reusable Space Vehicle Design Study Exploring Sharp Leading Edges," AIAA Paper 2001-2884, June 2001.
3. K. UPADHYA, J.-M. YANG and W. P. HOFFMAN, *The Amer. Ceram. Soc. Bull.* **76** (1997) 51.
4. L. KAUFMAN, "Boride Composites—A New Generation of Nose Cap and Leading Edge Materials for Reusable Lifting Reentry Systems," AIAA Paper 70-278, Feb. 1970.
5. E. V. CLOUGHERTY, R. L. POBER and L. KAUFMAN, *Trans. Metall. Soc. AIME* **242** (1968) 1077.
6. W. C. TRIPP, H. H. DAVIS and H. C. GRAHAM, *Ceram. Bull.* **52** (1973) 612.
7. J. BULL. in 19th Conference on Composite Materials and Structures 157 (CIAC, Cocoa Beach, FL, 1995).
8. A. G. METCALFE, N. B. ELSNER, D. T. ALLEN, E. WUCHINA, M. OPEKA and E. OPILA, *Electrochem. Soc. Proc.* **99**(38) (1999) 489.
9. I. G. TALMY, J. A. ZAYKOSKI and M. A. OPEKA, *Ceram. Engng. Sci. Proc.* **19** (1998) 104.
10. P. KOLODZIEJ, J. BULL, J. SALUTE and D. L. KEESE, "First Flight Demonstration of a Sharp Ultra-High Temperature Ceramic Nosetip," NASA TM-112215, Dec. 1997.

11. J. BULL, P. KOLODZIEJ, J. SALUTE and D. KEESE, "Design, Instrumentation and Preflight Testing of a Sharp Ultra-High Temperature Ceramic Nosetip," NASA TM-1998-112229, Oct. 1998.
12. T. KOBAYASHI and D. A. SHOCKEY, *Adv. Mater. Proc.* **140** (1991) 28.
13. ANON, "Standard Test Method for Monotonic Equibiaxial Flexural Strength of Advanced Ceramics at Ambient Temperature," ASTM C 1499-03, July 2003.
14. B. LAWN and R. WILSHAW, *J. Mater. Sci.* **10** (1975) 1049.
15. A. G. EVANS and T. R. WILSHAW, *Acta Metall.* **24** (1976) 939.
16. D. R. CLARKE and K. T. FABER, *J. Phys. Chem. Solids* **48** (1987) 1115.
17. B. R. LAWN and M. V. SWAIN, *J. Mater. Sci.* **10** (1975) 113.
18. B. R. LAWN, T. JENSEN and A. ARORA, *J. Mater. Sci. Lett.* **11** (1976) 573.
19. B. R. LAWN and E. R. FULLER, *J. Mater. Sci.* **10** (1975) 2016.
20. A. G. EVANS, *J. Amer. Ceram. Soc.* **56** (1973) 405.
21. B. R. LAWN, S. M. WIEDERHORN and H. H. JOHNSON, *ibid.* **58** (1975) 428.
22. C. G. KNIGHT, M. V. SWAIN and M. M. CHAUDHRI, *J. Mater. Sci.* **12** (1977) 1573.
23. S. M. WIEDERHORN and B. R. LAWN, *J. Amer. Ceram. Soc.* **60** (1977) 451.
24. W. H. RHODES, E. V. CLOUGHERTY and D. KALISH, "Research and Development of Refractory Oxidation-Resistant Diborides, Part II, Vol. IV: Mechanical Properties," AFML-TR-68-190, Jan. 1970.
25. V. E. LYSAGHT and A. DEBELLIS, "Hardness Testing Handbook" (American Chain and Cable Company, 1969).
26. Y. V. MILMAN, B. A. GALANOV and S. I. CHUGUNOVA, *Acta Metallurgica et Materialia* **41** (1993) 2523.
27. L. BSENKO and T. LUNDSTRÖM, *J. Less-Comm. Met.* **34** (1974) 273.
28. K. NAKANO, H. MATSUBARA and T. IMURA, *ibid.* **47** (1976) 259.
29. V. M. GLAZOV and V. N. VIGDOROVICH, "Microhardness of Metals and Semiconductors" (Consultants Bureau, New York, 1971).
30. G. D. QUINN, P. J. PATEL and I. LLOYD, *J. Res. National Inst. Stand. Techn.* **107** (2002) 299.
31. A. KAKANAKOVA-GEORGIEVA, E. P. TRIFONOVA, R. YAKIMOVA, M. F. MACMILLAN and E. JANZÉN, *Cryst. Res. Techn.* **34** (1999) 943.

Received 5 November 2003
and accepted 9 February 2004